

CrossMark  
click for updates

Cite this: DOI: 10.1039/c6ta02722a

# Efficiency and long-term durability of a nitrogen-doped single-walled carbon nanotube electrocatalyst synthesized by defluorination-assisted nanotube-substitution for oxygen reduction reaction†

Koji Yokoyama,<sup>a</sup> Shun Yokoyama,<sup>a</sup> Yoshinori Sato,<sup>b</sup> Kazutaka Hirano,<sup>b</sup> Shinji Hashiguchi,<sup>b</sup> Kenichi Motomiya,<sup>a</sup> Hiromichi Ohta,<sup>c</sup> Hideyuki Takahashi,<sup>a</sup> Kazuyuki Tohji<sup>a</sup> and Yoshinori Sato<sup>\*ad</sup>

Nitrogen-doped carbon nanomaterials are known to be excellent electrocatalysts for the oxygen reduction reaction (ORR) in polymer electrolyte fuel cells. In this study, we used a new and simple post-doping synthesis method to prepare nitrogen-doped single-walled carbon nanotubes (SWCNTs) by reacting fluorinated SWCNTs with ammonia gas at 300–600 °C. The structure and morphology of the N<sub>x</sub>C-doped SWCNTs (x: reaction temperature) synthesized by the defluorination-assisted nanotube-substitution reaction were characterized. Their levels of nitrogen doping (1.38–3.04 at%) are fairly high, with enriched pyridinic- and pyrrolic-nitrogen species. Their electrochemical catalytic activity for ORR in 0.5 M H<sub>2</sub>SO<sub>4</sub> was evaluated by cyclic voltammetry and linear sweep voltammetry, and their catalytic durability was assessed in load-potential cycle tests. For the N<sub>x</sub>C-doped SWCNTs, the peak and the onset potential ( $E_{\text{peak}}$  and  $E_{\text{onset}}$ , respectively) shifted towards the positive and the current density ( $j@E_{1/2}$ ) at the half-wave potential ( $E_{1/2}$ ) increased with increasing reaction temperature. The  $E_{\text{onset}}$  values of N<sub>500°C</sub>- and N<sub>600°C</sub>-doped SWCNTs were +0.51 V while that of the non-fluorinated hc-SWCNTs was +0.16 V. The number of electrons transferred per oxygen molecule ( $n$ ) in ORR was determined to be 2.32–3.64 at the potential of –0.3 V. The ORR catalytic activity was evaluated comprehensively through the measured parameters  $E_{\text{peak}}$ ,  $E_{\text{onset}}$ ,  $n$ , and  $j@E_{1/2}$ . The N<sub>500°C</sub>-doped SWCNTs possessed the highest ORR catalytic activity. After 11 000 cycles in the load-potential test, its current density remained at 93% of the initial value, indicating better durability than platinum nanoparticles supported on carbon black (Pt–C).

Received 1st April 2016  
Accepted 11th May 2016

DOI: 10.1039/c6ta02722a

www.rsc.org/MaterialsA

<sup>a</sup>Graduate School of Environmental Studies, Tohoku University, Aoba 6-6-20, Aramaki, Aoba-ku, Sendai 980-8579, Japan. E-mail: yoshinori.sato.bs5@tohoku.ac.jp; Fax: +81-22-795-3215; Tel: +81-22-795-3215

<sup>b</sup>Stella Chemifa Corporation, 1-41, Rinkai-cho, Izumiotsu, Osaka 595-0075, Japan

<sup>c</sup>Research Institute for Electronic Science, Hokkaido University, N20W10, Kita, Sapporo 001-0020, Japan

<sup>d</sup>Institute for Biomedical Sciences, Interdisciplinary Cluster for Cutting Edge Research, Shinshu University, Asahi 3-1-1, Matsumoto 390-8621, Japan

† Electronic supplementary information (ESI) available: (1) Preparation of hc-SWCNTs, (2) synthesis of F<sub>2.69at%</sub>- and F<sub>5.62at%</sub>-SWCNTs, (3) CV and LSV measurement procedures, (4) models of nitrogen positions in the structure, (5) wide-range and narrow N<sub>1s</sub> XPS spectra of the hc-SWCNTs after reaction with NH<sub>3</sub> gas at 500 °C, (6) chemical composition of the hc-SWCNTs after reaction with NH<sub>3</sub> gas at 500 °C, (7) wide-range XPS spectrum of the F<sub>2.69at%</sub>- and F<sub>5.62at%</sub>-SWCNTs, (8) chemical composition of the F<sub>2.69at%</sub>- and F<sub>5.62at%</sub>-SWCNTs, (9) CV and RDE curves of the F<sub>2.69at%</sub>- and F<sub>5.62at%</sub>-SWCNTs/GC electrodes, (10)  $E_{\text{peak}}$ ,  $j_{\text{peak}}$ ,  $E_{\text{onset}}$ ,  $j@E_{1/2}$ , and  $n$  value involved in ORR for the F<sub>2.69at%</sub>- and F<sub>5.62at%</sub>-SWCNT catalysts, (11) ECSA-cycle number plot of the Pt–C catalyst, (12) CV curves of the Pt–C catalytic electrode in N<sub>2</sub>-saturated 0.5 M H<sub>2</sub>SO<sub>4</sub> electrolyte before and after the durability test. See DOI: 10.1039/c6ta02722a

## 1. Introduction

Fuel cells have many advantages compared to conventional power sources. In polymer electrolyte fuel cells (PEFCs), catalysts for the oxygen reduction reaction (ORR) on the cathode are crucial for cell power performance.<sup>1,2</sup> Platinum nanoparticles supported on carbon black (Pt–C) have been regarded as the standard ORR catalyst.<sup>3</sup> However, the high and volatile price of Pt significantly increases the cost of PEFCs, making their large-scale adoption difficult. In addition, the coarsening of Pt nanoparticles during the dissolution/reprecipitation cycles<sup>4,5</sup> and the oxidative corrosion of carbon black due to a rapid potential variation in the high potential area<sup>4,6</sup> can decrease the activity of Pt–C in the PEFCs, leading to a shorter cell lifetime. Consequently, in recent years there has been great interest in developing cheap, durable, and Pt-free ORR catalysts with sufficiently high performance to replace Pt–C.<sup>7,8</sup> In particular, nitrogen-doped carbon nanomaterials, such as nitrogen-doped carbon nanofibers,<sup>9,10</sup> nitrogen-doped carbon alloys,<sup>11–13</sup>

nitrogen-doped carbon black,<sup>14</sup> nitrogen-doped graphenes,<sup>15–17</sup> nitrogen-doped carbon nanotubes (CNTs),<sup>18–20</sup> and nitrogen-doped CNT–graphene complexes,<sup>21</sup> have been reported to exhibit excellent electrocatalytic activity for the ORR.

In nitrogen-doped carbon nanomaterials, the active sites for the ORR are believed to be either pyridinic-type<sup>18,22–27</sup> or graphitic-type nitrogen atoms.<sup>12,28–30</sup> A universal understanding of the relationship between nitrogen doping and the resulting ORR catalytic activity is still unavailable. Meanwhile, multi-walled CNTs (MWCNTs) with hole defects on the walls,<sup>31</sup> as well as defective air-oxidized MWCNTs,<sup>32</sup> have also exhibited high ORR activity. The edges and defects, which exist in most reported nitrogen-doped carbon nanomaterials, may also serve as ORR active sites. In contrast, single-walled carbon nanotubes (SWCNTs) have a carbon lattice with  $sp^2$  hybridized bonds without edges, defects, or stacked graphene structures, and thus can serve as a model material for studying the ORR active sites. In nitrogen-doped SWCNTs, controlling the structural factors (*e.g.*, the level of nitrogen doping, the chemical bonding state, and the regularity of the carbon lattice structure after doping) is key to identifying the catalytic active sites.

Existing methods for doping CNTs with nitrogen are generally categorized into the “direct-doping” and “post-doping” syntheses.<sup>33</sup> The direct-doping synthesis can be realized through either the arc discharge method<sup>34,35</sup> or the chemical vapor deposition (CVD) method.<sup>36–40</sup> The majority of reported nitrogen-doped CNTs used as ORR catalysts are synthesized by the CVD method. However, in both methods it is extremely hard to control the structural factors mentioned above. Meanwhile, post-doping synthesis, in which nitrogen atoms are introduced to the synthesized/formed CNTs, allows one to control these structural factors.<sup>41,42</sup> However, the preparation of SWCNTs with high levels of nitrogen doping and preserved SWCNT lattice structure using the post-doping approach has not been reported.

Recently, we succeeded in synthesizing nitrogen-doped SWCNTs by defluorination-assisted nanotube-substitution reaction.<sup>43</sup> In this new post-doping synthesis method, fluorinated SWCNTs were reacted with ammonia gas at reaction temperatures of 300–600 °C. The maximum level of nitrogen doping in the prepared materials was 3.04 at%, and the two functional groups “pyridinic-nitrogen (Pyri-N) and pyrrolic-nitrogen (Pyrr-N)” and “graphitic-nitrogen (Grap-N)” accounted for 72–76% and 16–19% of the total nitrogen species, respectively. In the current study, we investigated the ORR catalytic activity of these nitrogen-doped SWCNTs by cyclic voltammetry (CV) and linear sweep voltammetry (LSV), using the rotating disk electrode (RDE) technique in an aqueous sulfuric acid electrolyte. The durability of these catalysts was also evaluated and shown to surpass that of the Pt–C catalyst.

## 2. Experimental section

### 2.1. Synthesis of nitrogen-doped SWCNTs

Fig. 1 is a schematic illustration of the synthesis procedure of the nitrogen-doped SWCNTs synthesized by the defluorination-assisted nanotube-substitution reaction with ammonia gas at

reaction temperatures of 300–600 °C.<sup>43</sup> Highly crystalline SWCNTs (hc-SWCNTs) were synthesized by the arc discharge method, purified by oxidation in air and a subsequent acid treatment, and finally annealed at 1200 °C (for details see “Preparation of hc-SWCNTs” in the ESI†).<sup>43–45</sup> Next, the fluorination procedure was carried out as follows: 150 mg of the hc-SWCNTs were put in a polytetrafluoroethylene (PTFE) tube (inner diameter of 6.0 mm). The PTFE tube was then placed at the center of a stainless steel tube (inner diameter of 10 mm), which, in turn, was kept at the center of a tubular electric furnace. After the hc-SWCNTs had been annealed in vacuum at 250 °C for 2 h in order to remove the water adsorbed on them, they were fluorinated at 250 °C using a gas mixture of 20%  $F_2/N_2$  for 4 h (flow rate of 25 mL  $min^{-1}$ ). Subsequently, they were subjected to thermal annealing at 250 °C for 1 h in a nitrogen flow (20 mL  $min^{-1}$ ). The fluorinated SWCNTs were characterized using X-ray photoelectron spectroscopy (XPS). From the XPS data, their C : F stoichiometry was determined to be  $CF_{0.39}$ . These fluorinated SWCNTs are hereafter referred to as “F-SWCNTs”. The final procedure for the nitrogen-doping reaction was as follows: 10 mg of the F-SWCNTs was put in a quartz glass boat, and the boat was placed at the center of a quartz glass tube (inner diameter of 21.4 mm and length of 700 mm), which was then set at the center of a tubular electric furnace. After the F-SWCNTs had been annealed in vacuum at 110 °C for 1 h in order to remove the water adsorbed on them, they were held in vacuum until the temperature at the centre of the furnace reached certain reaction temperatures (at steps of 100 °C for temperatures of 300–600 °C). Next, the F-SWCNTs were reacted with ammonia at the specific temperature for 30 min in a flow of a mixture of 1.0%  $NH_3/N_2$  gas (flow rate of 250 mL  $min^{-1}$ ). After the completion of the reaction, the sample was allowed to cool to room temperature in a nitrogen gas flow (50 mL  $min^{-1}$ ) and was subsequently removed from the furnace. These nitrogen-doped SWCNTs are hereafter referred to as “ $N_{x-C}$ -doped SWCNTs” ( $x$ : reaction temperature).

### 2.2. Characterization of materials

XPS was performed using an AXIS-ULTRA system (Shimadzu Ltd, Japan) with a monochromatized Al K $\alpha$  line in order to analyze the elemental composition and chemical bonding state of the samples. The sample morphologies were determined using a HRTEM system (HF-2000, Hitachi, Japan) equipped with a field-emission gun. The HRTEM systems were operated at 200 kV. Raman scattering spectroscopy (Jobin-Yvon T64000, Horiba Co. Ltd, Japan) was used to analyze the vibrational modes of the graphitic materials. These measurements were performed at room temperature using a semiconducting laser (473.0 nm). The specific Brunauer–Emmett–Teller (BET) surface area was measured on an Autosorb-iQ (Quantachrome Instruments, USA) by nitrogen molecule adsorption at –196 °C.

### 2.3. ORR catalytic activity test

CV and LSV were used to evaluate the ORR activity of the sample catalysts, using the RDE technique with an analytical rotator system (RRDE-1, NikkoKeisoku, Japan). The CV and LSV

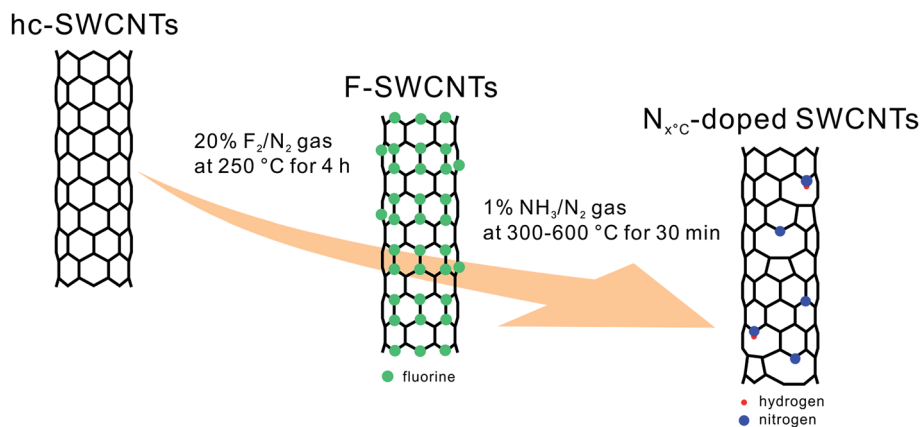


Fig. 1 Schematic illustration of the defluorination-assisted nanotube-substitution reaction for the synthesis of nitrogen-doped SWCNTs.

measurements were obtained using a potentiostat/galvanostat (Reference 600, Gamry Instruments, USA) in a single-compartment glass cell with an assembled three-electrode arrangement. The working electrodes were glassy carbon electrodes ( $\varphi = 6$  mm) embedded in Teflon (NDE-4, NikkoKeisoku, Japan). These electrodes were polished on polishing cloth to obtain a mirror surface, using two different alumina slurries with grain diameters of 1.0 and 0.05  $\mu\text{m}$  (BAIKALOX, Baikowski, France). A platinum ring was used as the counter electrode, and the potential of the working electrode was measured using an Ag/AgCl

(saturated KCl) reference electrode. All potentials described in this study are based on the Ag/AgCl reference electrode (+0.199 V vs. RHE). A 0.5 M  $\text{H}_2\text{SO}_4$  solution was used as the electrolyte, which was prepared from high-purity sulfuric acid (Semiconductor Grade, Wako Pure Chemical Industries, Ltd, Japan) and ultrapure water (PURELAB flex system, ELGA, USA; resistivity = 18.2  $\text{M}\Omega$  cm; TOC  $\leq$  5 ppb). Each measurement was carried out in both  $\text{N}_2$ - and  $\text{O}_2$ -saturated electrolytes obtained from purging with the respective gases ( $\text{N}_2$ : purity > 99.9995 vol%

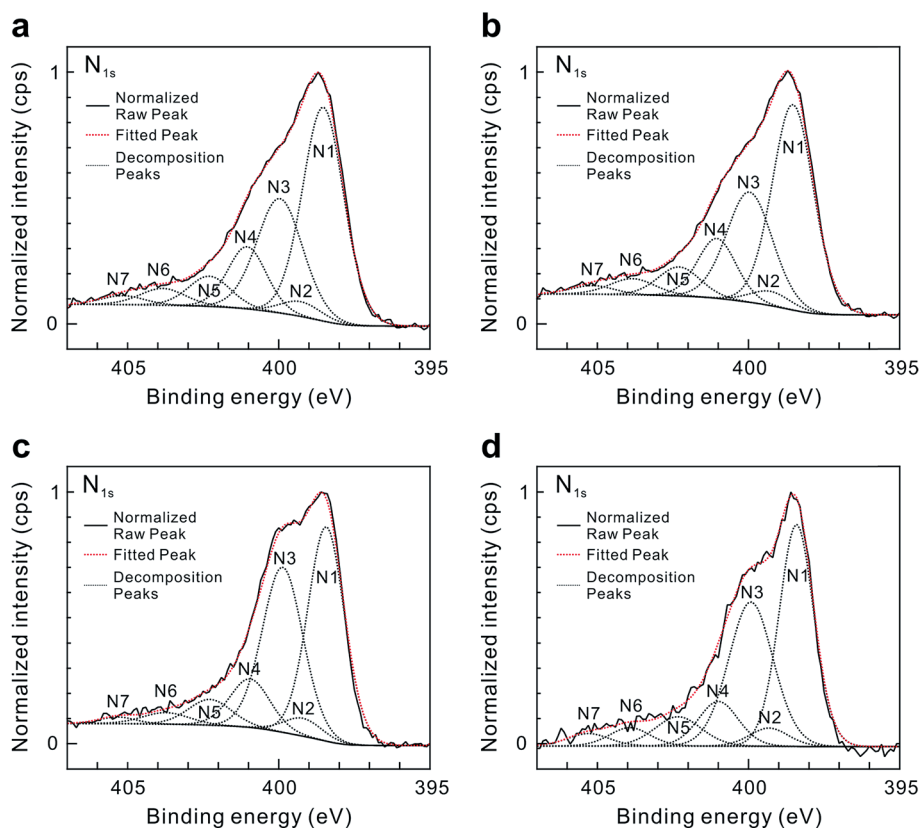


Fig. 2  $\text{N}_{1s}$  XPS spectra of the (a)  $\text{N}_{300^\circ\text{C}}$ -doped, (b)  $\text{N}_{400^\circ\text{C}}$ -doped, (c)  $\text{N}_{500^\circ\text{C}}$ -doped, and (d)  $\text{N}_{600^\circ\text{C}}$ -doped SWCNTs. The dotted lines are the deconvoluted peaks N1–N7.

(G3 grade), O<sub>2</sub>: purity > 99.9 vol% (G3 grade). Both from Taiyo Nippon Sanso Co., Japan) for over 30 min.

The catalytic inks were prepared by mixing N<sub>x</sub>C-doped SWCNTs (synthesized at x°C), 5 wt% Nafion solution (DE521 CS, Wako Pure Chemical Industries, Ltd, Japan), and ethanol (HPLC Grade, Wako Pure Chemical Industries, Ltd, Japan) in the mass ratio of 1 : 1 : 20 and sonicating for 30 min. The catalytic layer was created by drop-casting 12 μL catalytic ink on the GC electrode followed by sufficient drying at room temperature. Then, a mixture of 5 wt% Nafion solution and ethanol (in 1 : 10 weight ratio) was used to coat a thin Nafion layer on top of the catalytic layer, by dropping 6 μL of the Nafion/ethanol solution on the catalyst/GC electrode and drying sufficiently at room temperature. The thin Nafion layer acts as a binder to prevent the deposited catalytic layer from detaching from the GC electrode. This layer can also reduce the internal resistance of the catalyst electrode.<sup>46,47</sup> The amount of the catalyst and the thickness of the Nafion layer on the electrode were estimated to be 1.55 mg cm<sup>-2</sup> and 0.38 μm, respectively.<sup>46</sup>

The non-doped SWCNTs (hc-SWCNTs) and commercial Pt-C catalysts with 46.1 wt% Pt (TEC10E50E, Tanaka Kikinzoku Kogyo, Japan) were used as comparisons. Their CV and LSV curves were recorded with catalytic electrodes prepared with the same procedure and layer structure. For the Pt-C catalyst, the LSV curves were recorded in the potential range of -0.1 to +1.0 V. The procedures of the CV and LSV measurements are explained in the ESI.† All measurements were performed at 25 ± 1 °C and repeated three times for verification.

#### 2.4. Durability test of ORR catalytic activity

The durability of nitrogen-doped carbon nanomaterials for ORR has been measured in many ways, such as against CO or CH<sub>3</sub>OH impurities in the gases,<sup>18,48</sup> current stability tests at constant potentials,<sup>25,49</sup> and electrochemical stability tests by continuous CV.<sup>21,48,50</sup> In this study, the catalytic durability of N<sub>x</sub>C-doped SWCNTs and Pt-C catalysts was examined by a load cycle test in potential cycle tests recommended by the Fuel Cell Commercialization Conference of Japan (FCCJ).<sup>51</sup> The catalytic electrode on RDE, which is not a membrane-electrode assembly but a single catalytic electrode (half-cell), was prepared in the same way as for the CV and LSV measurements. The potential step cycling test was performed in N<sub>2</sub>-saturated 0.5 M H<sub>2</sub>SO<sub>4</sub> without

rotation. For the hc- and N<sub>x</sub>C-doped SWCNT catalytic electrodes, in each cycle the potential was stepped between +0.4 and +0.8 V, with a holding period of 3 s at each step. After every 1000 cycles, the electrolyte was saturated with oxygen by bubbling with O<sub>2</sub> for over 30 min, and the LSV curve was then recorded (scan rate: 10 mV s<sup>-1</sup>, potential range: -0.3 to +0.8 V, rotation rate: 1600 rpm). For the Pt-C catalytic electrode, the tests were conducted under the same conditions except that the LSV curves were recorded in the potential range of +0.1 to +1.0 V. The percentage decrease in the current density of ORR at a standard potential in the LSV curves was used as the durability indicator.<sup>49</sup> In the FCCJ recommendation, the current density at +0.9 V vs. RHE (+0.7 V vs. Ag/AgCl in saturated KCl) in the LSV curve at the rotation rate of 1600 rpm is the standard potential for Pt-C catalysts.<sup>51</sup> In this study, the current density of Pt-C catalyst electrodes at +0.7 V was 80% that of the limiting current density in the LSV curve. Therefore, the standard potential for the N-doped SWCNT catalyst is defined as the potential at which its current density is 80% the respective limiting current density in the LSV curve. After every 1000 cycles, a CV scan was conducted at the scan rate of 10 mV s<sup>-1</sup> in the potential range of -0.15 to +1.0 V in the N<sub>2</sub>-saturated electrolyte. The electrochemically active surface area (ECSA) was estimated from the area integral of the hydrogen absorption/desorption curves. The durability test was stopped when this area decreased to less than 50% of its initial value before the test.<sup>51</sup>

## 3. Results and discussion

### 3.1. Characterization of nitrogen-doped SWCNTs

The N<sub>1s</sub> XPS peak for each N<sub>x</sub>C-doped SWCNT sample could be deconvoluted into seven peaks (Fig. 2). The peaks labeled N1, N2, N3, N4, and N5 were attributable to the pyridinic-type nitrogen bond (398.5 ± 0.1 eV),<sup>41,52</sup> primary amine bond (399.3 ± 0.1 eV),<sup>43,45,53</sup> pyrrolic-type nitrogen bond (400.0 ± 0.2 eV),<sup>41,52</sup> graphitic-type nitrogen bond with the center-nitrogen atom (401.2 ± 0.1 eV, for the nitrogen position see the model in Fig. S1a†),<sup>29,41,52</sup> and the graphitic-type nitrogen bond with the valley-nitrogen atom (402.4 ± 0.1 eV, for the nitrogen position see the model in Fig. S1b†).<sup>29</sup> The XPS peaks labeled N6 (403.9 ± 0.2 eV) and N7 (405.3 ± 0.2 eV) with higher binding energies were assigned to nitrogen oxide groups such as pyridine-N-oxide

**Table 1** Chemical compositions of the hc-, F-, and N<sub>x</sub>C-doped SWCNTs and the respective concentrations of various nitrogen species, as estimated from the XPS results. The ratios of the Raman scattering intensities (*I*<sub>D</sub>/*I*<sub>G</sub>) between the D-band and G-band, and the BET specific surface areas for each sample are also shown

| Samples                          | Chemical composition (at%) |      |      |       | Component of nitrogen species (at%) |      |      |      |      |      |      | <i>I</i> <sub>D</sub> / <i>I</i> <sub>G</sub> | BET (m <sup>2</sup> g <sup>-1</sup> ) |
|----------------------------------|----------------------------|------|------|-------|-------------------------------------|------|------|------|------|------|------|---|---------------------------------------|
|                                  | C                          | O    | N    | F     | N1                                  | N2   | N3   | N4   | N5   | N6   | N7   |   |                                       |
| hc-SWCNTs                        | 98.48                      | 1.52 | 0.00 | 0.00  | —                                   | —    | —    | —    | —    | —    | —    | 0.01 ± 0.001                                  | 173.4 ± 22.3                          |
| F-SWCNTs                         | 71.36                      | 1.11 | 0.00 | 27.53 | —                                   | —    | —    | —    | —    | —    | —    | 0.92 ± 0.042                                  | 151.3 ± 10.6                          |
| N <sub>300</sub> °C-doped SWCNTs | 87.16                      | 1.67 | 2.64 | 8.53  | 1.19                                | 0.08 | 0.71 | 0.33 | 0.17 | 0.10 | 0.05 | 0.69 ± 0.057                                  | 173.0 ± 7.83                          |
| N <sub>400</sub> °C-doped SWCNTs | 94.20                      | 1.62 | 3.04 | 1.14  | 1.28                                | 0.09 | 0.92 | 0.37 | 0.20 | 0.10 | 0.08 | 0.56 ± 0.020                                  | 173.0 ± 21.4                          |
| N <sub>500</sub> °C-doped SWCNTs | 95.19                      | 1.63 | 2.38 | 0.80  | 0.98                                | 0.08 | 0.84 | 0.24 | 0.14 | 0.07 | 0.03 | 0.56 ± 0.050                                  | 181.0 ± 23.0                          |
| N <sub>600</sub> °C-doped SWCNTs | 96.49                      | 1.22 | 1.38 | 0.91  | 0.55                                | 0.05 | 0.46 | 0.13 | 0.10 | 0.05 | 0.04 | 0.56 ± 0.062                                  | 208.9 ± 13.4                          |

bond and nitro groups.<sup>29,54,55</sup> Table 1 summarizes the chemical compositions and concentrations of the various nitrogen species in each sample obtained from the XPS analysis. The concentration of nitrogen doping was in the range of 1.38–3.04 at%, with the maximum doping occurring in the N<sub>400°C</sub>-doped SWCNTs. Therefore, this method is effective for introducing nitrogen atoms at high concentrations. From Table 1, all the N<sub>x°C</sub>-doped SWCNTs contained enriched pyridinic- and pyrrolic-types of nitrogen (72–76%) and graphitic-type nitrogen (16–19%). The hc-SWCNTs were directly reacted with 1.0% NH<sub>3</sub>/N<sub>2</sub> mixed gas (*i.e.*, without fluorination) at 300–600 °C (at steps of 100 °C) for 30 min. Fig. S2† shows the wide-range and narrow N<sub>1s</sub> XPS spectra of the hc-SWCNTs after reaction at 500 °C. No peaks related to the nitrogen chemical bonds were detected by XPS (see Table S1†). Therefore, the defluorination-assisted nanotube-substitution reaction is the key for doping nitrogen into the carbon framework at relatively low temperature.

Fig. 3 shows the high resolution transmission electron microscopy (HRTEM) images of each sample. The straight lattice in the hc-SWCNTs is clearly visible, indicating their highly crystalline structure (Fig. 3a). In Fig. 3b, the lattice in the F-SWCNTs with the chemical composition of CF<sub>0.39</sub> is also quite visible, therefore the carbon framework remained intact during fluorination. In the N<sub>x°C</sub>-doped SWCNTs (Fig. 3c–f), the linearity and clarity of the lattice decreased with increasing reaction temperature, indicating the formation of wavy, disordered turbostratic structures with nanoscale vacancy-type defects. In

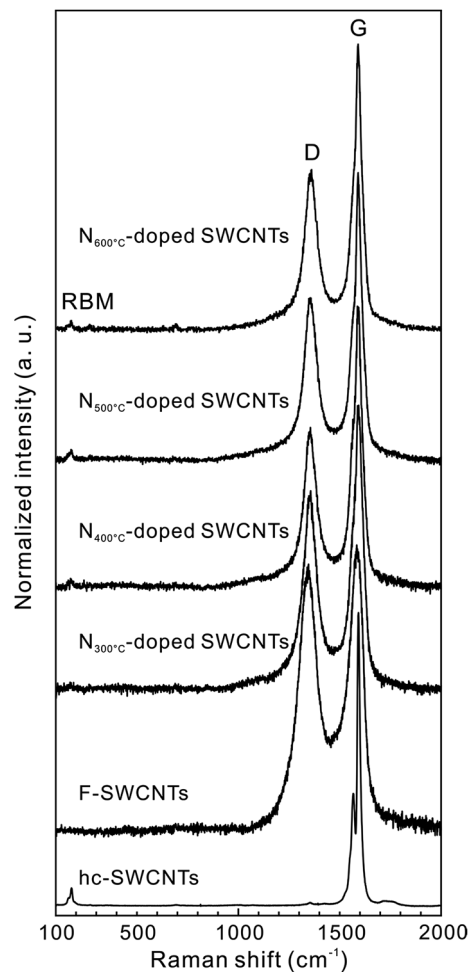


Fig. 4 Raman scattering spectra of the samples. From bottom up: hc-, F-, N<sub>300°C</sub>-doped, N<sub>400°C</sub>-doped, N<sub>500°C</sub>-doped, and N<sub>600°C</sub>-doped SWCNTs.

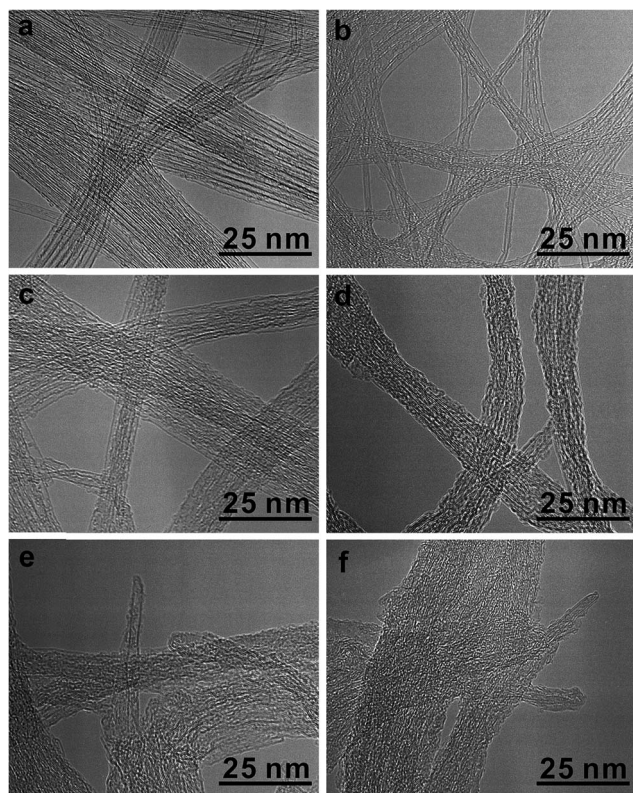


Fig. 3 HRTEM images of the (a) hc-, (b) F-, (c) N<sub>300°C</sub>-doped, (d) N<sub>400°C</sub>-doped, (e) N<sub>500°C</sub>-doped, and (f) N<sub>600°C</sub>-doped SWCNTs.

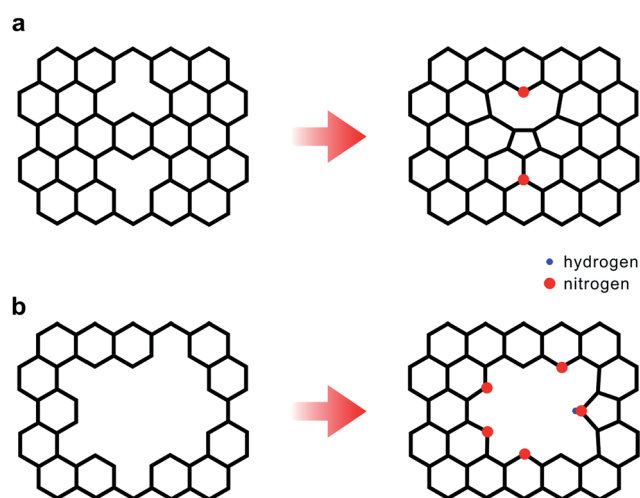


Fig. 5 Schematic models of skeletal reconstruction of the carbon frame by nitrogen doping in the cases of (a) small hole defects and (b) large hole defects created during defluorination.

particular, the edge faces, which occur in the cross-section of bundled nanotubes, were observed in the  $N_{500^\circ\text{C}}$ - and  $N_{600^\circ\text{C}}$ -doped SWCNTs.

In the Raman spectra of the samples (Fig. 4), the high ratio ( $I_D/I_G$ ) of the intensities between the D band ( $1350\text{ cm}^{-1}$ ) and the G band ( $1590\text{ cm}^{-1}$ ) for F-SWCNTs indicated that a large amount of fluorine groups and a small amount of oxygen-containing groups were introduced into the nanotubes, and that they bonded with the carbon atoms on the nanotube frame through  $\text{sp}^3$ -hybridized covalent bonds (Table 1). For  $N_{x^\circ\text{C}}$ -doped SWCNTs, the  $I_D/I_G$  value at  $x = 300$  ( $0.691 \pm 0.057$ ) was higher than that at other temperatures because of the remaining fluorine groups (8.53 at%). The  $I_D/I_G$  values of other  $N_{x^\circ\text{C}}$ -doped SWCNTs were approximately 0.560, which is higher

than that of hc-SWCNTs. The reason can be explained as follows. The intensity of the D band can be increased by two factors: an increased number of topological defects formed by defluorination, and framework distortions such as the turbostratic and wavy structure due to the different bond lengths between C–C and C–N in the nanotube frame of the  $N_{x^\circ\text{C}}$ -doped SWCNTs.<sup>56</sup> At high reaction temperatures (500 and 600 °C), a large number of  $\text{C}_x\text{F}_y$  molecules such as  $\text{C}_2\text{F}_6$ ,  $\text{C}_3\text{F}_7$ , and  $\text{C}_4\text{F}_7$  became detached.<sup>45,57,58</sup> This process induced large topological defects and edges in the carbon framework. However, the nitrogen content decreased with increasing reaction temperature, as shown in Table 1. As a result, the  $I_D/I_G$  of the  $N_{500^\circ\text{C}}$ - and  $N_{600^\circ\text{C}}$ -doped SWCNTs were similar to that doped at 400 °C, because at higher reaction temperature the number of edges

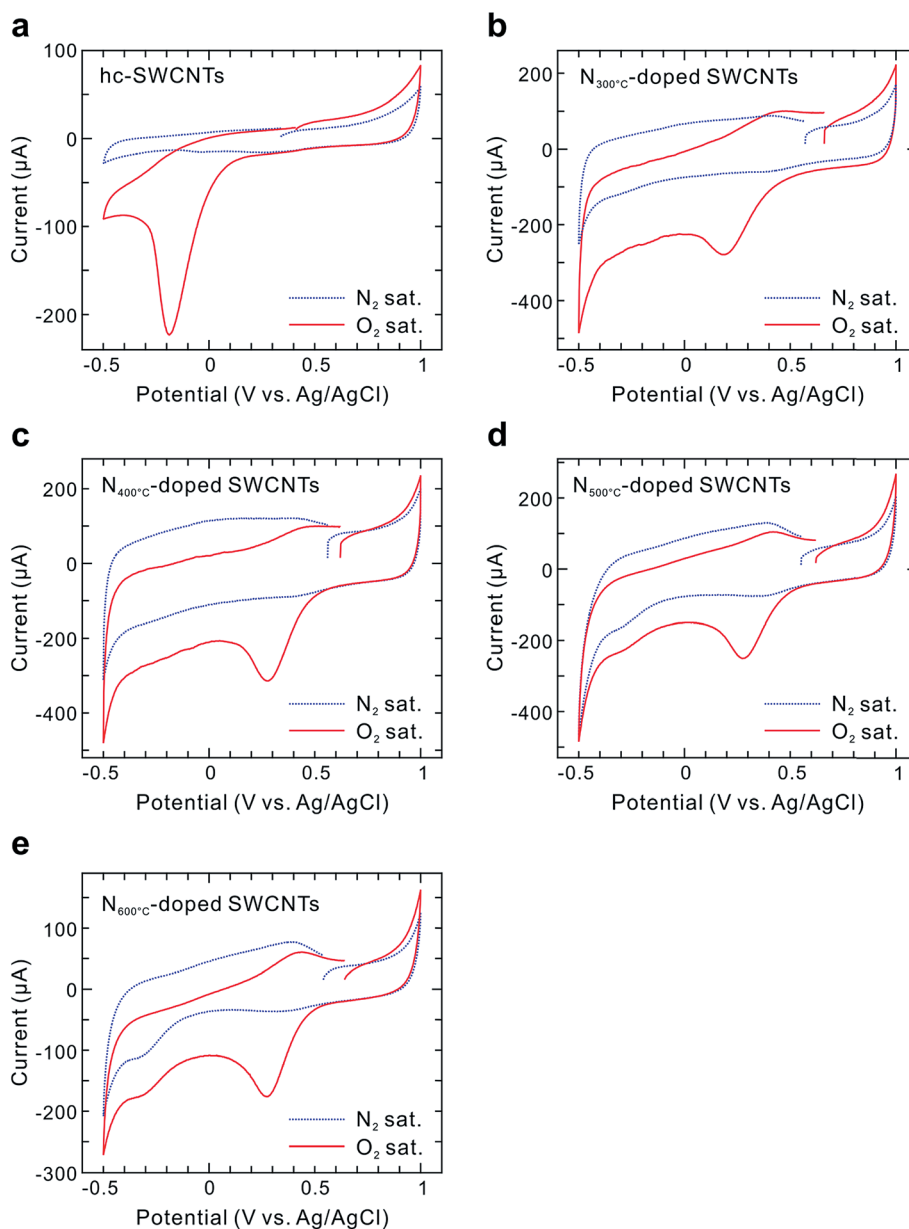


Fig. 6 Cyclic voltammograms of the (a) hc-, (b)  $N_{300^\circ\text{C}}$ -doped, (c)  $N_{400^\circ\text{C}}$ -doped, (d)  $N_{500^\circ\text{C}}$ -doped, and (e)  $N_{600^\circ\text{C}}$ -doped SWCNTs/GC electrodes in  $\text{N}_2$ -saturated (blue dotted line) and  $\text{O}_2$ -saturated (red solid line) 0.5 M  $\text{H}_2\text{SO}_4$  electrolyte (scan rate:  $10\text{ mV s}^{-1}$ ).

increased while the framework distortions from the C–N bond decreased. In the F- and N<sub>300°C</sub>-doped SWCNTs, we did not detect any peaks of the radial breathing mode (RBM), because RBM in the nanotube frame was hindered by the remaining fluorine groups.<sup>59</sup> In other N<sub>x°C</sub>-doped SWCNTs, a weak RBM peak was detected at the same position as in hc-SWCNTs, showing that the nanotube frame remained tubular after doping.

The BET specific surface area of hc-SWCNTs with 4.0–40 nm in bundle diameter was  $173 \pm 22.3 \text{ m}^2 \text{ g}^{-1}$  (Table 1), while the reported value for bundled SWCNTs is about  $200 \text{ m}^2 \text{ g}^{-1}$ .<sup>60</sup> The specific surface area of F-SWCNTs decreased to  $151.3 \pm 10.6 \text{ m}^2 \text{ g}^{-1}$ , due to the increase in sample weight by the functionalization of fluorine groups. The specific surface areas of N<sub>500°C</sub>- and N<sub>600°C</sub>-doped SWCNTs were slightly higher than that of the hc-SWCNTs, due to the nanoscopic defects and deformations in these two samples.

When the F-SWCNTs were heated at temperatures of 300–600 °C, the fluorine groups were detached along with carbon atoms from the nanotube frame in the form of C<sub>x</sub>F<sub>y</sub>,<sup>45,57,58</sup> leaving topological defects. Small vacancy-type defects spanning one or two carbon atoms can be repaired by the introduced nitrogen atoms such as Pyri-N and Grap-N (Fig. 5a). With large vacancy-type defects, in contrast, Pyri-N and Pyrr-N are believed to be introduced only to the edges of the defects, while the defects themselves are not repaired (Fig. 5b). Since the contents of the Pyri-N and Pyrr-N were high in the N<sub>x°C</sub>-doped SWCNT samples, large vacancy-type defects are expected to exist, which are possibly related to the highly concentrated fluorine groups. Gu *et al.* reported that the fluorination of purified SWCNTs (HiPco) to the stoichiometry of CF<sub>0.2</sub> followed by pyrolysis at up to 1000 °C breaks the nanotubes to short segments of various lengths.<sup>61</sup> They speculated that such segmentation is related to the distribution of fluorine atoms on the walls of the SWCNTs. Scanning tunneling microscopy analysis of fluorinated SWNTs<sup>62</sup> revealed that the fluorine atoms tend to arrange themselves around the circumference of the nanotubes to form fluorine-rich bands. In partially fluorinated SWNTs, the transition between the fluorinated and non-fluorinated bands typically remains orthogonal

to the SWNT axis.<sup>62</sup> As the pyrolysis affects only the fluorinated parts of the wall while leaving the non-fluorinated parts intact, this band-like structure causes the SWNTs to break into shorter sections. The F-SWCNTs in this study possess a high degree of fluorination (with a stoichiometry CF<sub>0.39</sub>), therefore the fluorine groups may also be concentrated in certain regions, where large vacancy-type defects are formed after defluorination. If both the concentration and location of the fluorine groups in F-SWCNTs can be controlled with precision, the types and concentration of the nitrogen sites after nitrogen-doping will also be controlled.

### 3.2. ORR catalytic activity

The CV curves of all samples are shown in Fig. 6. All the catalytic electrodes exhibited ORR activity in the presence of oxygen, while no response was observed in the same potential range in the N<sub>2</sub>-saturated electrolyte. The hc-SWCNT electrode showed a peak potential ( $E_{\text{peak}}$ ) at  $-0.2 \text{ V}$ , therefore it is not a good ORR catalyst. This is consistent with previous reports on the ORR catalytic activity of non-nitrogen doped carbon materials in acidic media.<sup>24,63</sup> The average  $E_{\text{peak}}$  values of the N<sub>300°C</sub>-, N<sub>400°C</sub>-, N<sub>500°C</sub>-, and N<sub>600°C</sub>-doped SWCNTs were  $+0.19$ ,  $+0.27$ ,  $+0.27$ , and  $+0.26 \text{ V}$ , respectively (Table 2).  $E_{\text{peak}}$  of the N<sub>x°C</sub>-doped SWCNTs shifted to more positive values compared to the non-doped sample, with a maximum shift of  $0.47 \text{ V}$ . The average current densities ( $j_{\text{peak}}$ ) at  $E_{\text{peak}}$  (after subtracting the background value in the N<sub>2</sub>-saturated electrolyte) were  $-0.68$ ,  $-0.67$ ,  $-0.76$ ,  $-0.60$ , and  $-0.52 \text{ mA cm}^{-2}$ , respectively (Table 2).

Fig. 7 shows the RDE curves obtained at different rotation rates, and Fig. 8 compares the LSV curves of all samples at 1600 rpm. From these curves, the onset potential ( $E_{\text{onset}}$ ) and the current density ( $j@E_{1/2}$ ) at the half-wave potential ( $E_{1/2}$ ) were estimated.  $E_{\text{onset}}$  is defined as the potential where the current density reaches  $10 \mu\text{A cm}^{-2}$ .<sup>25</sup> To quantify the reaction, the number of electrons transferred per oxygen molecule in the ORR process was determined by the Koutecky–Levich equation (eqn (1)), which relates the current density  $j$  to the rotation rate of the electrode  $\omega$ :

$$\frac{1}{j} = \frac{1}{j_k} + \frac{1}{B\omega^{1/2}} \quad (1)$$

**Table 2** Peak potential ( $E_{\text{peak}}$ ), peak current density ( $j_{\text{peak}}$ ), onset potential ( $E_{\text{onset}}$ ), current density at half-wave potential ( $j@E_{1/2}$ ), and number of electrons transferred per oxygen molecule ( $n$ ) involved in ORR for the hc-, N<sub>x°C</sub>-doped SWCNTs, and Pt–C catalysts

| Materials                        | CV                    |  | RDE                    |                                    |                   |                   |
|----------------------------------|-----------------------|--|------------------------|------------------------------------|-------------------|-------------------|
|                                  | $E_{\text{peak}}$ (V) | $j_{\text{peak}}$ (mA cm <sup>-2</sup> ) | $E_{\text{onset}}$ (V) | $j@E_{1/2}$ (mA cm <sup>-2</sup> ) | $n$               |                   |
| hc-SWCNTs                        | -0.20                 | -0.68                                    | +0.16                  | ND <sup>a</sup>                    | ND <sup>b</sup>   | 2.32 <sup>d</sup> |
| N <sub>300°C</sub> -doped SWCNTs | +0.18                 | -0.67                                    | +0.43                  | -1.88                              | 2.79 <sup>c</sup> | 2.91 <sup>d</sup> |
| N <sub>400°C</sub> -doped SWCNTs | +0.27                 | -0.76                                    | +0.50                  | -2.13                              | 2.93 <sup>c</sup> | 2.85 <sup>d</sup> |
| N <sub>500°C</sub> -doped SWCNTs | +0.27                 | -0.60                                    | +0.51                  | -1.82                              | 3.31 <sup>c</sup> | 3.17 <sup>d</sup> |
| N <sub>600°C</sub> -doped SWCNTs | +0.26                 | -0.52                                    | +0.51                  | -1.62                              | 3.39 <sup>c</sup> | 3.64 <sup>d</sup> |
| Pt–C                             | +0.64                 | +0.99                                    | +0.85                  | -2.78                              | 4.00 <sup>e</sup> | 4.00 <sup>e</sup> |

<sup>a</sup> Indicates “no estimation” because the limit diffusion current density cannot be observed. <sup>b</sup> Indicates “no estimation” because the linear correlation of the Koutecky–Levich plot at a potential of  $-0.1 \text{ V}$  cannot be provided. <sup>c</sup> Indicates values taken at a potential of  $-0.1 \text{ V}$ . <sup>d</sup> Indicates values taken at a potential of  $-0.3 \text{ V}$ . <sup>e</sup> Indicates values taken at a potential ranging from  $0.1$  to  $0.6 \text{ V}$ .

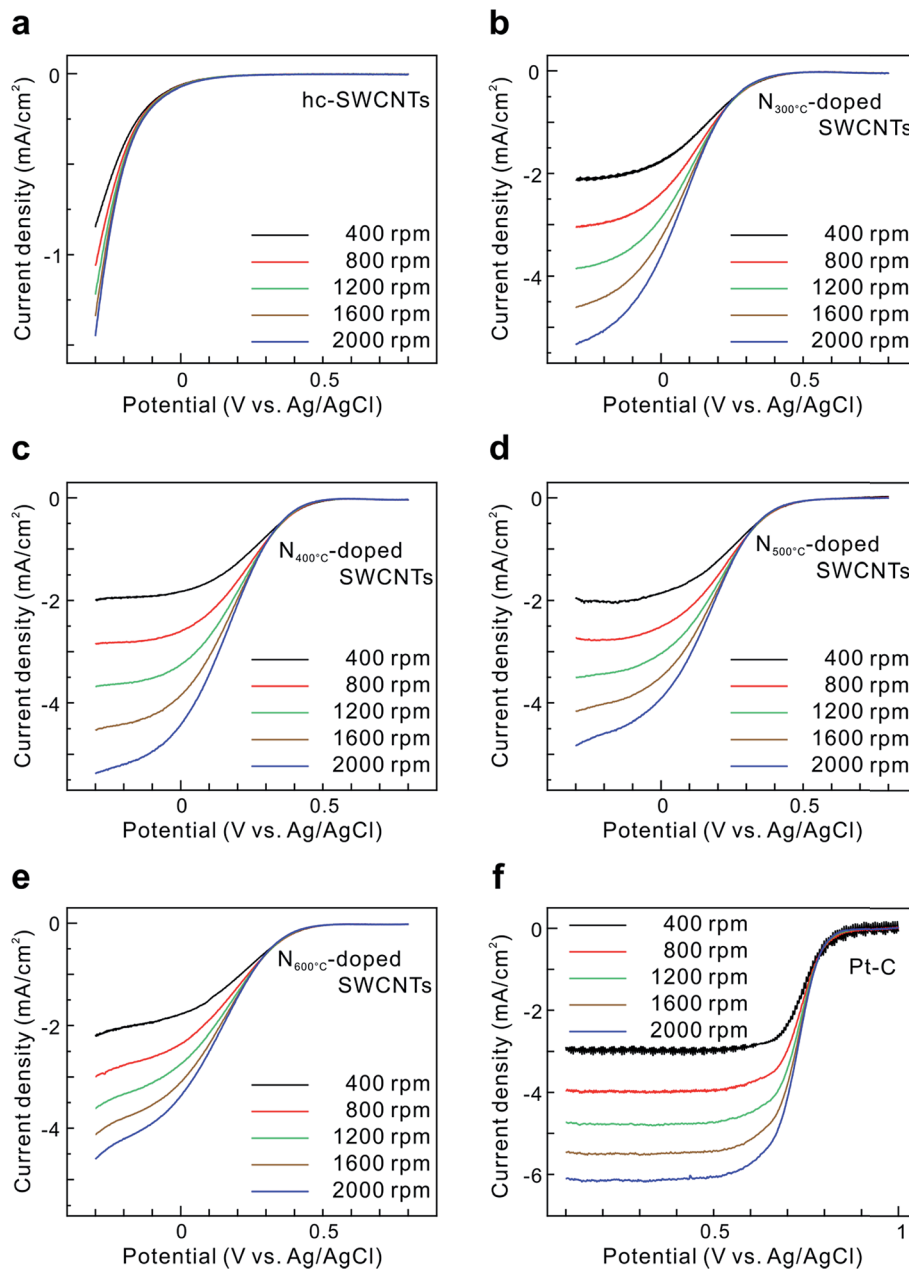


Fig. 7 RDE curves for oxygen reduction with (a) hc-, (b) N<sub>300°C</sub>-doped, (c) N<sub>400°C</sub>-doped, (d) N<sub>500°C</sub>-doped, (e) N<sub>600°C</sub>-doped SWCNTs, and (f) commercial Pt-C on GC electrodes in O<sub>2</sub>-saturated 0.5 M H<sub>2</sub>SO<sub>4</sub> electrolyte (scan rate: 10 mV s<sup>-1</sup>, rotation rate: 400–2000 rpm in increments of 400 rpm).

where  $j_k$  is the kinetic current density,  $B$  is the Levich slope related to the diffusion-limiting current density, and  $j$  is the observed current density at the rotation speed  $\omega$ . The Levich slope can be calculated as:

$$B = 0.62nFC_{O_2}(D_{O_2})^{2/3}\nu^{-1/6} \quad (2)$$

where  $n$  is the number of electrons transferred per oxygen molecule,  $F$  is the Faraday constant,  $C_{O_2}$  is the bulk oxygen concentration in the electrolyte,  $D_{O_2}$  is the diffusion coefficient of oxygen, and  $\nu$  is the viscosity of the electrolyte. In 0.5 M H<sub>2</sub>SO<sub>4</sub> solution,  $C_{O_2}$  is  $1.4 \times 10^{-6}$  mol cm<sup>-3</sup>,  $D_{O_2}$  is  $1.15 \times 10^{-5}$  cm<sup>2</sup> s<sup>-1</sup>,

and  $\nu$  is  $1.07 \times 10^{-2}$  cm<sup>2</sup> s<sup>-1</sup>.<sup>19</sup> The value of  $n$  can be determined from the slope in the Koutecky-Levich plot at each potential using eqn (2). The average  $E_{onset}$ ,  $j@E_{1/2}$ , and  $n$  for all samples are summarized in Table 2.  $E_{onset}$  shifts to the positive in the N<sub>x°C</sub>-doped SWCNTs with increasing reaction temperature. The value of  $E_{onset}$  for the N<sub>500°C</sub>-doped and N<sub>600°C</sub>-doped SWCNTs was +0.51 V, while that of hc-SWCNTs was +0.16 V. The current density at the half-wave potential,  $j@E_{1/2}$ , was undetectable in the hc-SWCNTs, as the limiting current was not observed in the LSV curve. In contrast,  $j@E_{1/2}$  of the N<sub>400°C</sub>-doped SWCNTs reached a maximum at  $-2.13$  mA cm<sup>-2</sup>. The value of  $n$  at the potential of  $-0.3$  V for the hc-SWCNT electrode is 2.32,

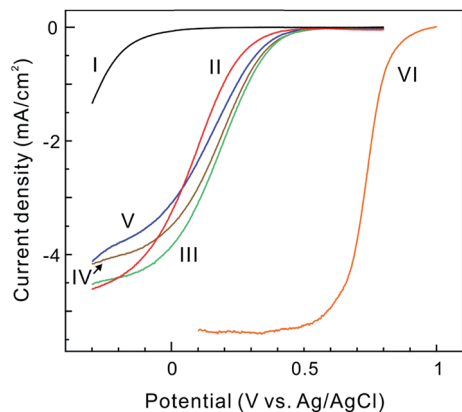


Fig. 8 Linear sweep voltammograms of (I) hc-, (II)  $N_{300^\circ\text{C}}$ -doped, (III)  $N_{400^\circ\text{C}}$ -doped, (IV)  $N_{500^\circ\text{C}}$ -doped, (V)  $N_{600^\circ\text{C}}$ -doped SWCNTs, and (VI) commercial Pt-C on GC electrodes in  $\text{O}_2$ -saturated 0.5 M  $\text{H}_2\text{SO}_4$  electrolyte (scan rate:  $10 \text{ mV s}^{-1}$ , rotation rate: 1600 rpm).

indicating the dominance of the two-electron pathway, which is an inefficient ORR with oxygen reduced to water through hydrogen peroxide ( $\text{H}_2\text{O}_2$ ). On the other hand, for the  $N_{x^\circ\text{C}}$ -doped SWCNTs  $n$  increased with increasing reaction temperature, with  $n > 3$  for the  $N_{500^\circ\text{C}}$ - and  $N_{600^\circ\text{C}}$ -doped SWCNT

electrodes at  $-0.3 \text{ V}$ . In particular,  $n$  for the  $N_{600^\circ\text{C}}$ -doped SWCNTs was as high as 3.64. Therefore, in these two samples the four-electron pathway, which is an efficient ORR that directly reduces oxygen to water, is dominant with the coexisting two-electron pathway.<sup>24,32</sup>

For the four  $N_{x^\circ\text{C}}$ -doped SWCNT catalysts, Fig. 9a presents the contents of residual fluorine groups and  $E_{\text{onset}}$ , while Fig. 9b presents the contents of residual fluorine groups and  $n$  values. The residual fluorine content, which decreases with increasing reaction temperature, is inversely correlated with  $E_{\text{onset}}$  and  $n$ . A larger amount of fluorine groups in fluorinated SWCNTs reduces the contribution to  $\pi$  electron conductivity from the  $\text{sp}^2$ -covalently bonded carbon atoms.<sup>64</sup> As previously reported, the average volume resistivity of each free-standing  $N_{x^\circ\text{C}}$ -doped SWCNT film was in the 1.9 to 3.7  $\Omega \text{ cm}$  range, indicating that their resistivities were almost the same.<sup>43</sup> Therefore, a larger number of residual fluorine groups in the  $N_{300^\circ\text{C}}$ -doped SWCNTs are considered not to lead to a higher internal resistance in the catalyst electrode. Sun *et al.* reported that fluorine-doped carbon black with a fluorine content of 0.41 at% had enhanced catalytic activity for ORR in 0.1 M KOH.<sup>65</sup> Here, we evaluated the ORR catalytic activity of nitrogen-free fluorinated SWCNTs with two different fluorine contents (2.69 and 5.62 at%, respectively) by CV and RDE curves in 0.5 M  $\text{H}_2\text{SO}_4$

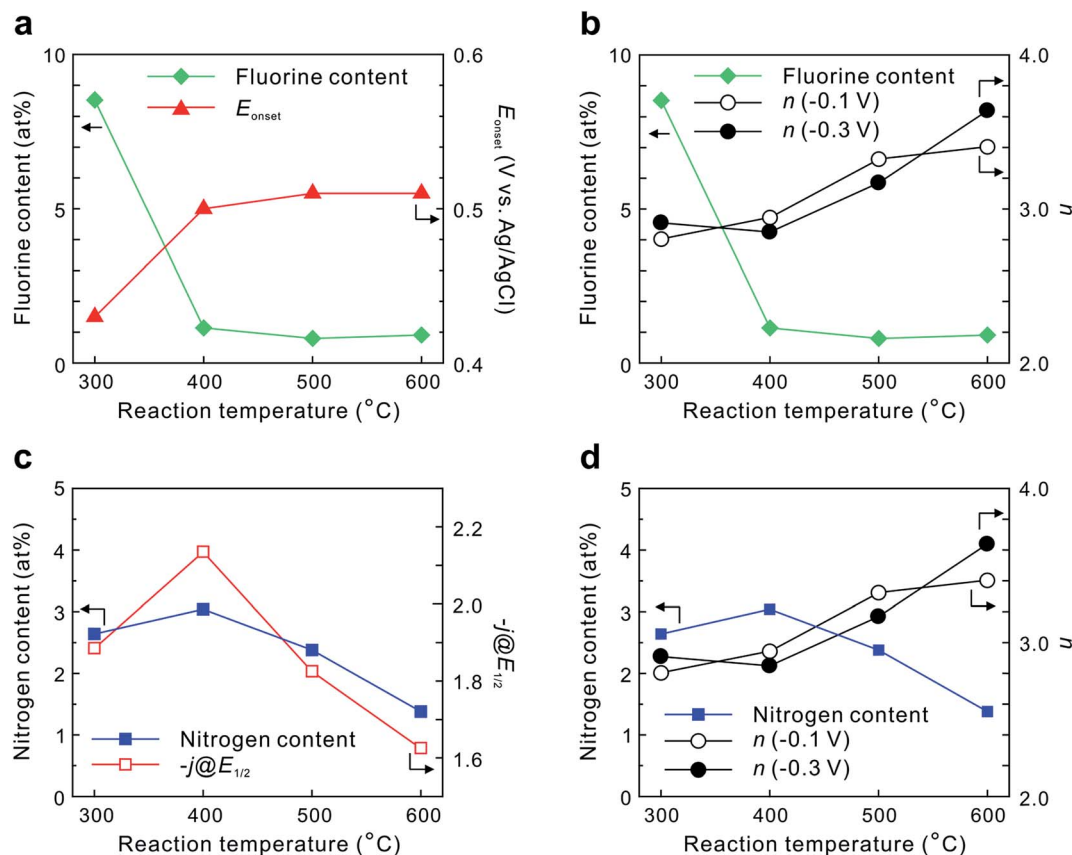


Fig. 9 (a) Fluorine content and the onset potential as functions of the reaction temperature in  $N_{x^\circ\text{C}}$ -doped SWCNTs. (b) Residual fluorine content and the number of electrons transferred per oxygen molecule in ORR as functions of the reaction temperature. (c) Nitrogen content and the oxygen reduction current density at half-wave potential as functions of the reaction temperature. (d) Nitrogen content and the number of electrons transferred per oxygen molecule in ORR as functions of the reaction temperature.

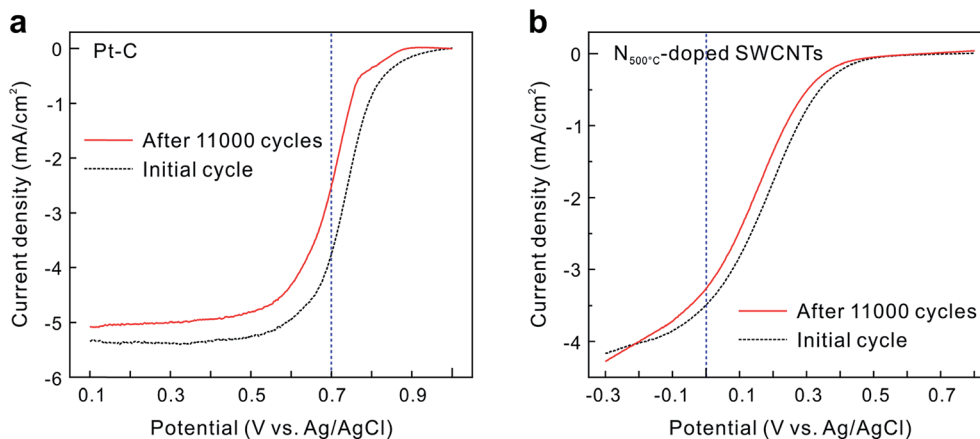


Fig. 10 Linear sweep voltammograms of (a) commercial Pt-C and (b)  $N_{500^\circ\text{C}}$ -doped SWCNTs on GC electrodes in  $\text{O}_2$ -saturated 0.5 M  $\text{H}_2\text{SO}_4$  electrolyte, both before and after the durability test (scan rate:  $10 \text{ mV s}^{-1}$ , rotation rate: 1600 rpm). The blue vertical line is the respective standard potential.

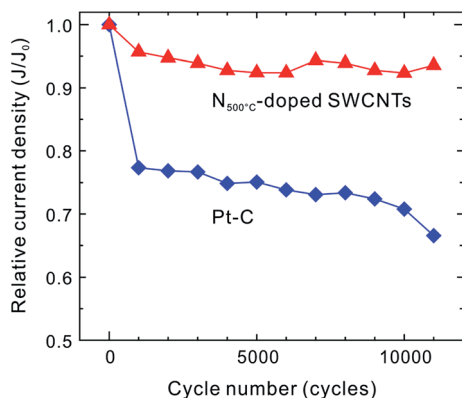


Fig. 11 Relative current densities of  $N_{500^\circ\text{C}}$ -doped SWCNTs and commercial Pt-C during 11 000 cycles of the durability test.

(referred to as “ $F_{2.69\text{at}\%}$ -SWCNTs” and “ $F_{5.62\text{at}\%}$ -SWCNTs”; see “Materials and methods”, Fig. S3, and Table S2 in the ESI†). The  $F_{2.69\text{at}\%}$ -SWCNT catalyst exhibited low ORR activity because the  $E_{\text{peak}}$ ,  $E_{\text{onset}}$ , and  $n$  value were respectively  $-0.09 \text{ V}$ ,  $+0.23 \text{ V}$ , and 2.46 (Fig. S4 and Table S3†), which are comparable to or slightly higher than those for the hc-SWCNT catalyst. In addition, the  $F_{5.62\text{at}\%}$ -SWCNT catalyst also showed low ORR activity. The fluorine groups of both the  $F_{2.69\text{at}\%}$ - and  $F_{5.62\text{at}\%}$ -SWCNTs do not have a good effect on ORR activity in 0.5 M  $\text{H}_2\text{SO}_4$ . Therefore, the fluorine groups are the likely reason why the  $N_{300^\circ\text{C}}$ -doped SWCNTs had lower ORR catalytic activity than those doped at higher temperatures ( $400$ – $600^\circ\text{C}$ ). Fig. 9c presents the correlation between the content of the introduced nitrogen atoms and  $j@E_{1/2}$ , while Fig. 9d presents the content of the introduced nitrogen atoms and the corresponding  $n$  values, as the reaction temperature is varied. This correlation shows that the doping nitrogen atoms increase the ORR catalytic active sites, leading to increased  $j@E_{1/2}$ . However, the  $n$  value of the  $N_{600^\circ\text{C}}$ -doped SWCNT catalyst is higher than that of  $N_{500^\circ\text{C}}$ -doped SWCNT catalyst. At this stage, we speculate this phenomenon as follows. In the  $N_{x^\circ\text{C}}$ -doped SWCNTs

( $x = 500, 600$ ), the  $n$  values are close to 4 with decreasing nitrogen contents. In these catalyst samples prepared at higher temperatures, a number of large topological defects with their associated edges were created, at which a small number of pyridinic- and pyrrolic-type nitrogen atoms could be introduced. Although the samples had lower  $j@E_{1/2}$  values, these nitrogen functionalities (species) might play a key role in the four-electron pathway for the ORR. In an effort to clarify the ORR catalytic active sites, we need to control the content and species of doping nitrogen atoms in nitrogen-doped SWCNTs.

Judged from the  $E_{\text{peak}}$ ,  $E_{\text{onset}}$ ,  $n$ , and  $j@E_{1/2}$  values in a comprehensive manner, the  $N_{500^\circ\text{C}}$ -doped SWCNT catalyst in this study possessed the highest ORR catalytic activity. Its ORR activity is comparable to previously reported values for nitrogen-doped SWCNTs in the same electrolyte.<sup>19</sup>

### 3.3. Durability of ORR catalytic activity

The ECSA value of the Pt-C catalyst was reduced to 50% of the initial value after 11 000 cycles (Fig. S5a†). Therefore, the durability test was limited to 11 000 cycles. (The CV curves of the Pt-C catalytic electrode before and after the potential cycle test are shown in Fig. S5b.†) Fig. 10 shows the LSV curves of the  $N_{500^\circ\text{C}}$ -doped SWCNTs, which exhibited the best ORR catalytic activity, and the Pt-C catalyst before and after the durability test. The current densities of both catalysts were found to decrease after the test. Fig. 11 shows the relative ORR current density of each catalyst electrode during potential cycling, normalized by the initial current density at the respective standard potential. At the 11 000<sup>th</sup> cycle, the relative current density of Pt-C was only 67% of its initial value, and its ECSA value decreased as well. In contrast, 93% of the initial current density of  $N_{500^\circ\text{C}}$ -doped SWCNTs was maintained at the 11 000<sup>th</sup> cycle, demonstrating its excellent durability in the load-potential cycle for ORR catalytic activity. We believe such excellent durability can be attributed to the preservation of the nanotube frame and the high content of nitrogen-doped sites.

## 4. Conclusions

We have developed a new and simple post-doping synthesis method to synthesize nitrogen-doped SWCNTs by reacting fluorinated SWCNTs with ammonia gas at reaction temperatures of 300–600 °C. In this study, the prepared metal-free nitrogen-doped SWCNTs were evaluated for their electrochemical ORR catalytic activity by CV and LSV using the RDE technique, and their catalytic durability was compared to that of Pt–C in the load-cycle test in potential cycle tests in 0.5 M H<sub>2</sub>SO<sub>4</sub>. The N<sub>x</sub>-C-doped SWCNTs, especially the N<sub>500</sub>-C-doped sample, demonstrated excellent ORR catalytic activity, in terms of peak potential ( $E_{\text{peak}}$ ), onset potential ( $E_{\text{onset}}$ ), current density at the half-wave potential ( $j@E_{1/2}$ ), the number of electrons transferred ( $n$ ), and long-term catalytic durability.

Given the various advantages of the defluorination-assisted nanotube-substitution reaction, in the future we plan to synthesize nitrogen-doped SWCNTs with a better preserved nanotube frame, higher amounts of nitrogen doping, and controlled nitrogen species by optimizing the synthesis conditions, such as the degree of fluorination and the flow of ammonia gas. We believe these new carbon nanomaterials will exhibit even better ORR catalytic activity and durability, as well as provide clarification of the ORR catalytic active sites.

## Acknowledgements

Y. S. was supported by the Japan Society for the Promotion of Science (JSPS) KAKENHI Grant Number 25630290 and 15H04131. K. T. was supported by the JSPS KAKENHI Grant Number 26220104. H. O. was supported by the JSPS KAKENHI Grant Number 25106007 and 25246023. Finally, this work was also supported in part by the Network Joint Research Center for Materials and Devices, Japan.

## Notes and references

- M. V. Williams, H. R. Kunz and J. M. Fenton, *J. Electrochem. Soc.*, 2005, **152**, A635–A644.
- F. Jaouen, E. Proietti, M. Lefèvre, R. Chenitz, J.-P. Dodelet, G. Wu, H. T. Chung, C. M. Johnston and P. Zelenay, *Energy Environ. Sci.*, 2011, **4**, 114–130.
- P. Costamagna and S. Srinivasan, *J. Power Sources*, 2001, **102**, 242–252.
- X. Yu and S. Ye, *J. Power Sources*, 2007, **172**, 145–154.
- M. S. Wilson, F. H. Garzon, K. E. Sickafus and S. Gottesfeld, *J. Electrochem. Soc.*, 1993, **140**, 2872–2877.
- L. M. Roen, C. H. Paik and T. D. Jarvi, *Electrochem. Solid-State Lett.*, 2004, **7**, A19–A22.
- L. Zhang, J. Zhang, D. P. Wilkinson and H. Wang, *J. Power Sources*, 2006, **156**, 171–182.
- Z. L. Wang, D. Xu, H. X. Zhong, J. Wang, F. L. Meng and X. B. Zhang, *Sci. Adv.*, 2015, **1**, e1400035.
- P. H. Matter, L. Zhang and U. S. Ozkan, *J. Catal.*, 2006, **239**, 83–96.
- S. Maldonado and K. J. Stevenson, *J. Phys. Chem. B*, 2005, **109**, 4707–4716.
- J. Ozaki, T. Anahara, N. Kimura and A. Oya, *Carbon*, 2006, **44**, 3358–3361.
- H. Niwa, K. Horiba, Y. Harada, M. Oshima, T. Ikeda, K. Terakura, J. Ozaki and S. Miyata, *J. Power Sources*, 2009, **187**, 93–97.
- T. Ikeda, M. Boero, S.-F. Haung, K. Terakura, M. Oshima and J. Ozaki, *J. Phys. Chem. C*, 2008, **112**, 14706–14709.
- A. Zahoor, M. Christy, Y. J. Hwang, Y. R. Lim, P. Kim and K. S. Nahm, *Appl. Catal., B*, 2014, **147**, 633–641.
- D. Wei, Y. Liu, Y. Wang, H. Zhang, L. Huang and G. Yu, *Nano Lett.*, 2009, **9**, 1752–1758.
- L. Qu, Y. Liu, J.-B. Baek and L. Dai, *ACS Nano*, 2010, **4**, 1321–1326.
- H. X. Zhong, J. Wang, Y. W. Zhang, W. L. Xu, W. Xing, D. Xu, Y. F. Zhang and X. B. Zhang, *Angew. Chem., Int. Ed.*, 2014, **53**, 14235–14239.
- K. Gong, F. Du, Z. Xia, M. Durstock and L. Dai, *Science*, 2009, **323**, 760–764.
- D. Yu, Q. Zhang and L. Dai, *J. Am. Chem. Soc.*, 2010, **132**, 15127–15129.
- Z. L. Wang, D. Xu, J. J. Xu and X. B. Zhang, *Chem. Soc. Rev.*, 2014, **43**, 7746–7786.
- Y. Li, W. Zhou, H. Wang, L. Xie, Y. Liang, F. Wei, J.-C. Idrobo, S. J. Pennycook and H. Dai, *Nat. Nanotechnol.*, 2012, **7**, 394–400.
- S. Kundu, T. C. Nagaiah, W. Xia, Y. Wang, S. V. Dommele, J. H. Bitter, M. Santa, G. Grundmeier, M. Bron, W. Schuhmann and M. Muhler, *J. Phys. Chem. C*, 2009, **113**, 14302–14310.
- Z. Chen, D. Higgins, H. Tao, R. S. Hsu and Z. Chen, *J. Phys. Chem. C*, 2009, **113**, 21008–21013.
- N. Alexeyeva, E. Shulga, V. Kisand, I. Kink and K. Tammeveski, *J. Electroanal. Chem.*, 2010, **648**, 169–175.
- C. V. Rao, C. R. Cabrera and Y. Ishikawa, *J. Phys. Chem. Lett.*, 2010, **1**, 2622–2627.
- Z. Mo, S. Liao, Y. Zheng and Z. Fu, *Carbon*, 2012, **50**, 2620–2627.
- W. Y. Wong, W. R. W. Daud, A. B. Mohamad, A. A. H. Kadhum, K. S. Loh and E. H. Majlan, *Int. J. Hydrogen Energy*, 2013, **38**, 9421–9430.
- S. Ni, Z. Li and J. Yang, *Nanoscale*, 2012, **4**, 1184–1189.
- T. Sharifi, G. Hu and T. Wågberg, *ACS Nano*, 2012, **6**, 8904–8912.
- D. Srivastava, T. Susi, M. Borghei and L. Kari, *RSC Adv.*, 2014, **4**, 15225–15235.
- K. Waki, R. A. Wong, H. S. Oktaviano, T. Fujio, T. Nagai, K. Kimoto and K. Yamada, *Energy Environ. Sci.*, 2014, **7**, 1950–1958.
- M. Liu and J. Li, *Electrochim. Acta*, 2015, **154**, 177–183.
- Y. Zheng, Y. Jiao, M. Jaroniec, Y. Jin and S. Z. Qiao, *Small*, 2012, **8**, 3550–3566.
- R. Droppa Jr, P. Hammer, A. C. M. Carvalho, M. C. dos Santos and F. Alvarez, *J. Non-Cryst. Solids*, 2002, **299–302**, 874–879.
- M. Glerup, J. Steinmetz, D. Samaille, O. Stéphan, S. Enouz and A. Loiseau, *Chem. Phys. Lett.*, 2004, **387**, 193–197.

- 36 M. Yudasaka, R. Kikuchi, Y. Ohki and S. Yoshimura, *Carbon*, 1997, **35**, 195–201.
- 37 R. Sen, B. C. Satishkumar, A. Govindaraj, K. R. Harikumar, M. K. Renganathan and C. N. R. Rao, *J. Mater. Chem.*, 1997, **7**, 2335–2337.
- 38 R. Czerw, M. Terrones, J.-C. Charlier, X. Blasé, B. Foley, R. Kamalakaran, N. Grobert, H. Terrones, D. Tekleab, P. M. Ajayan, W. Blau, M. Rühle and D. L. Carroll, *Nano Lett.*, 2001, **1**, 457–460.
- 39 M. Terrones, P. M. Ajayan, F. Banhart, X. Blase, D. L. Carroll, J. C. Charlier, R. Czerw, B. Foley, N. Grobert and R. Kamalakaran, *Appl. Phys. A: Mater. Sci. Process.*, 2002, **74**, 355–361.
- 40 C. L. Pint, Z. Sun, S. Moghazy, Y. Q. Xu, J. M. Tour and R. H. Hauge, *ACS Nano*, 2011, **5**, 6925–6934.
- 41 S. Kundu, W. Xia, W. Busser, M. Becker, D. A. Schmidt, M. Havenith and M. Muhler, *Phys. Chem. Chem. Phys.*, 2010, **12**, 4351–4359.
- 42 Z. Jiang, A. Al-Zubaidi and S. Kawasaki, *Mater. Express*, 2014, **4**, 331–336.
- 43 K. Yokoyama, Y. Sato, K. Hirano, H. Ohta, K. Motomiya, K. Tohji and Y. Sato, *Carbon*, 2015, **94**, 1052–1060.
- 44 S. Iwata, Y. Sato, K. Nakai, S. Ogura, T. Okano, M. Namura, A. Kasuya, K. Tohji and K. Fukutani, *J. Phys. Chem. C*, 2007, **111**, 14937–14941.
- 45 K. Bushimata, S.-I. Ogino, K. Hirano, T. Yabune, K. Sato, T. Itoh, K. Motomiya, K. Yokoyama, D. Mabuchi, H. Nishizaka, G. Yamamoto, T. Hashida, K. Tohji and Y. Sato, *J. Phys. Chem. C*, 2014, **118**, 14948–14956.
- 46 E. Higuchi, H. Uchida and M. Watanabe, *J. Electroanal. Chem.*, 2005, **583**, 69–76.
- 47 M. Watanabe, H. Igarashi and K. Yosioka, *Electrochim. Acta*, 1995, **40**, 329–334.
- 48 S. Gouse Peera, A. K. Sahu, A. Arunchander, S. D. Bhat, J. Karthikeyan and P. Murugan, *Carbon*, 2015, **93**, 130–142.
- 49 J. Li, S. Wang, Y. Ren, Z. Ren, Y. Qiu and J. Yu, *Electrochim. Acta*, 2014, **149**, 56–64.
- 50 H. Zhong, H. Zhang, Z. Xu, Y. Tang and J. Mao, *ChemSusChem*, 2012, **5**, 1698–1702.
- 51 A. Iiyama, K. Shinohara, S. Iguchi and A. Daimaru, in *Handbook of Fuel Cells: Fundamentals Technology and Applications*, ed. W. Vielstich, H. Yokokawa and H. A. Gasteiger, John Wiley & Son, Ltd, Chichester, West Sussex, 2009, vol. 6, ch. 61, pp. 905–915.
- 52 L. G. Bulusheva, A. V. Okotrub, A. G. Kudashov, I. P. Asanov and O. G. Abrosimov, *Eur. Phys. J. D*, 2005, **34**, 271–274.
- 53 J. Lahaye, G. Nansé, A. Bagreev and V. Strelko, *Carbon*, 1999, **37**, 585–590.
- 54 H. Wang, R. Cote, G. Faubert, D. Guay and J. P. Dodelet, *J. Phys. Chem. B*, 1999, **103**, 2042–2049.
- 55 E. Raymundo-Piñero, D. Cazorla-Amorós, A. Linares-Solano, J. Find, U. Wild and R. Schlögl, *Carbon*, 2002, **40**, 597–608.
- 56 H. R. Barzegar, E. Gracia-Espino, T. Sharifi, F. Nitze and T. Wågberg, *J. Phys. Chem. C*, 2013, **117**, 25805–25816.
- 57 Y. M. Shulga, V. M. Martynenko, A. V. Krestinin, A. P. Kharitonov, G. I. Davidova, E. I. Knerelman, V. I. Krastev and D. V. Schur, *Int. J. Hydrogen Energy*, 2011, **36**, 1349–1354.
- 58 H. F. Bettinger and H. Peng, *J. Phys. Chem. B*, 2005, **109**, 23218–23224.
- 59 S. Kawasaki, K. Komatsu, F. Okino, H. Touhara and H. Kataura, *Phys. Chem. Chem. Phys.*, 2004, **6**, 1769–1772.
- 60 A. Fujiwara, K. Ishii, H. Suematsu, H. Kataura, Y. Maniwa, S. Suzuki and Y. Achiba, *Chem. Phys. Lett.*, 2001, **336**, 205–211.
- 61 Z. Gu, H. Peng, R. H. Hauge, R. E. Smalley and J. L. Margrave, *Nano Lett.*, 2002, **2**, 1009–1013.
- 62 K. F. Kelly, I. W. Chiang, E. T. Mickelson, R. H. Hauge, J. L. Margrave, X. Wang, G. E. Scuseria, C. Radloff and N. J. Halas, *Chem. Phys. Lett.*, 1999, **313**, 445–450.
- 63 N. Alexeyeva and K. Tammeveski, *Electrochim. Solid-State Lett.*, 2007, **10**, F18–F21.
- 64 P. E. Pehrsson, W. Zhao, J. W. Baldwin, C. Song, J. Liu, S. Kooi and B. Zheng, *J. Phys. Chem. B*, 2003, **107**, 5690–5695.
- 65 X. Sun, Y. Zhang, P. Song, J. Pan, L. Zhuang, W. Xu and W. Xing, *ACS Catal.*, 2013, **3**, 1726–1729.